

Direct Detection Under Tukey Signalling

Amir Tasbihi *Graduate Student Member, IEEE* and Frank R. Kschischang *Fellow, IEEE*

Abstract—A new direct-detection-compatible signalling scheme is proposed for fiber-optic communication over short distances. Controlled inter-symbol interference is exploited to extract phase information, thereby achieving spectral efficiencies about one bit less, per second per hertz, of those of a coherent detector.

Index Terms—direct detection, short-haul, ISI, Tukey window

I. INTRODUCTION

DIRECT detection or, synonymously, square-law detection, is a nonlinear waveform detection scheme based upon measuring the squared magnitude of a complex-valued waveform. It appears in various scientific fields, *e.g.*, crystallography [1], radio astronomy [2], [3], biomedical spectroscopy [4], detection and estimation theory [5]–[7], etc. This paper deals with the application of square-law detection in fiber-optic communication systems [8], [9], particularly those with short transmission length, *e.g.*, less than 10 km. Such systems occur, *e.g.*, in rack-to-rack data transmission within data centers.

Since square-law detectors base their decision only on the magnitude of the received complex-valued waveform—unlike coherent detectors which also access phase information—one might get the intuitive impression that the information rate of a communication channel under square-law detection should be roughly half the information rate of the same channel under coherent detection [10]–[13]. This intuition is actually correct for *intensity modulation with direct detection* (IM/DD) systems, which modulate only the magnitude of the transmitted waveform. In particular, the transmitted symbol in IM/DD systems belong to a finite real set whose elements have distinct intensity, *i.e.*, squared magnitude. Due to their simple transceiver structure, IM/DD systems have been extensively used in short-reach optical communications and have been investigated deeply in the literature [14]–[20]. However, the simplicity of IM/DD systems comes at the price of losing about half the degrees of freedom compared with coherent detection, which enables detection in the complex field.

Somewhat counter-intuitively, it can be shown that the capacity of waveform channels under square-law detection of bandlimited [21] and time-limited [22] signals is, in fact, at most one bit less, per second per hertz, than the capacity under coherent detection! Clearly, this is possible when the transmitted symbols may assume complex values. Thus, the price to pay for the convenience of direct detection may not be as high as intuition would suggest. Unfortunately, [21] and

[22] do not present a practical scheme to achieve the lower bound on the capacity derived in those papers.

Due to the simplicity of the receiver's optical front-end in direct detection, finding efficient communication schemes compatible with square-law detection is an active area of research. A popular recent scheme is the *Kramers–Kronig receiver* [23], which has been investigated thoroughly in the optical communication literature in the last few years. The Kramers–Kronig receiver enables recovery of a complex-valued waveform from its squared magnitude, which in turn enables the use of digital signal processors to mitigate dispersion, making direct detection viable for longer transmission lengths (> 100 km) than previously thought, where dispersion is a hindering factor [24]–[26]. These merits come with drawbacks however: a high required carrier-to-signal power ratio [27] and increased sampling rates necessitated by spectrum-broadening operations performed after the square-law device.

In this paper, a new direct-detection-compatible data transmission scheme is proposed that exploits deliberately-introduced inter-symbol interference (ISI) to extract phase information. The deliberate introduction of ISI in digital communication via so-called *partial-response coding* [28] dates back to the early 1960s, and allows for the design of line codes with prescribed spectral nulls and other useful properties [29]–[34]. Partial-response systems arise in high-density magnetic recording systems [35]–[37] where the read-channel is equalized to achieve a particular response characteristic. Deliberate intersymbol interference also arises in faster-than-Nyquist signalling schemes [38]–[41] which have been proposed for wireless and optical communications. In this paper we propose a new application of controlled ISI: namely, to extract phase information.

As a toy example to illustrate that ISI can be beneficial, let z_1 and z_2 be complex numbers. Then, from $|z_1|^2$, $|z_2|^2$, and $|z_1 + z_2|^2$ (an ISI term), one can retrieve the phase difference between z_1 and z_2 , up to a sign ambiguity.

As another example, let

$$g(t) = \sum_{\ell=0}^m g_{\ell} \operatorname{sinc}(t - \ell),$$

where $g_0, \dots, g_m \in \mathbb{C}$ and $\operatorname{sinc}(t) \triangleq \frac{\sin(\pi t)}{\pi t}$. Here $g(t)$ represents the signal transmitted in an ideal bandlimited quadrature amplitude modulation (QAM) data transmission system with unit symbol rate. Note that $|g(t)|^2 = g(t) \cdot g^*(t)$, being the product of bandlimited signals, has twice the bandwidth of $g(t)$, and thus there is a possibility to recover g_0, \dots, g_m from samples of $|g(t)|^2$ at $t = \frac{k}{2}$, where $k = 0, \dots, 2m$ (*i.e.*,

Submitted on May 26th, 2021; revised, July 11th, 2021. The authors are with the Edward S. Rogers Sr. Dept. of Electrical & Computer Engineering, University of Toronto, Toronto, ON M5S 3G4, Canada. Email: {tasbihi, frank}@ece.utoronto.ca.

samples taken at twice the symbol rate). Since

$$\left|g\left(\frac{k}{2}\right)\right|^2 = \begin{cases} \left|g_{\frac{k}{2}}\right|^2, & \text{if } k \text{ is even;} \\ \left|\sum_{\ell=0}^m g_{\ell} \operatorname{sinc}\left(\frac{k}{2} - \ell\right)\right|^2, & \text{if } k \text{ is odd,} \end{cases}$$

one can easily recover the magnitudes of g_0, \dots, g_m from the samples with an even k , while their phases are embedded in samples with an odd k . Unfortunately, since all g_{ℓ} 's contribute to the samples at half-integer times, recovering phase information is an intractable problem, even for moderately small values of m . Therefore, while ISI is useful to extract phase information, an excessive ISI would demand complex processing. This is the rationale for claiming that “controlled ISI” is needed.

The rest of the paper is organized as follows. The system model, including the transmitter, the channel, and the receiver, is described in Sec. II. In particular, the new signalling scheme is proposed in Sec. II-B. The scheme is validated via numerical simulations, whose results are given in Sec. III. The implementation complexity of the proposed scheme (in terms of digital-to-analog and analog-to-digital conversions per symbol) is compared with those of a coherent detector and a Kramers–Kronig detector in Sec. IV. Finally, concluding remarks are provided in Sec. V.

Throughout this paper, vectors are denoted by lower-case bold letters, *e.g.*, \mathbf{v} . For a vector \mathbf{v} of length m , $\mathbf{v}[k]$ denotes its k^{th} entry, where $k \in \{0, \dots, m-1\}$. The cardinality of a finite set \mathcal{A} is denoted by $|\mathcal{A}|$. The expected value and the variance of a random variable X are denoted as $\mathbb{E}[X]$ and $\operatorname{Var}(X)$, respectively. Likelihood functions will always be denoted as f , with arguments chosen to indicate the random variables involved; for example, the conditional probability density function of a random variable Y at a point $y \in \mathbb{R}$ given that a random variable X takes value x is denoted simply as $f(y|x)$ rather than the more cumbersome $f_{Y|X}(y|x)$. The notation $X \sim \mathcal{N}(\mu, \sigma^2)$ indicates that random variable X has a Gaussian distribution with mean μ and variance σ^2 . Finally, the positive real numbers are denoted as $\mathbb{R}^{>0}$.

II. THE SYSTEM MODEL

In this section we describe the system model, shown in Fig. 1. For simplicity and without loss of generality, we assume a complex baseband model.

A. Dispersion Precompensation & The Transmission Medium

As explained in Sec. I, the proposed scheme is aimed at short-range fiber-optic communications, *e.g.*, over a distance < 10 km. Therefore, to avoid amplified spontaneous-emission (ASE) noise, we assume an unamplified optical link. Indeed, we assume that the only source of noise is the photodiode, as discussed in Sec. II-C.

We assume that chromatic dispersion is precompensated at the transmitter using a precoder with transfer function $H(f) = e^{i2\beta_2 L \pi^2 f^2}$, where β_2 is the group-velocity dispersion parameter and L is the fiber length [42]–[46]. Therefore, the transmitted complex-valued waveform over the fiber is $u \triangleq \mathcal{F}^{-1}\{X(f)H(f)\}$, where $X(\cdot)$ is the Fourier transform

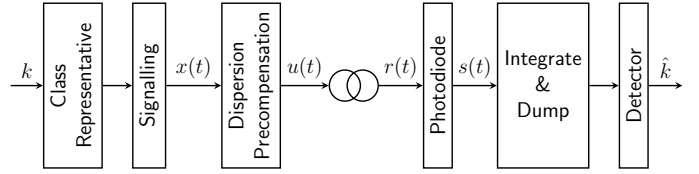


Fig. 1. The system model; $k \in \{1, \dots, M\}$, $x(\cdot)$, $u(\cdot)$, and $r(\cdot)$ are complex-valued waveforms, and $s(\cdot)$ is a real-valued waveform. As the chromatic dispersion is precompensated and the link is unamplified, we assume that $r(\cdot) = \rho x(\cdot)$, where $\rho \in (0, 1]$.

of $x(\cdot)$, the complex-valued input waveform of the all-pass filter, and \mathcal{F}^{-1} denotes the inverse Fourier transform operator. As the precoder is an all-pass filter, $x(\cdot)$ and $u(\cdot)$ have equal energy, thus dispersion precompensation does not result in a precoding loss, which is a drawback of some partial-response coding techniques, *e.g.*, Tomlinson-Harashima precoding [47]–[49].

As the optical-fiber length is relatively short, except for power loss, we dismiss other transmission impairments, *e.g.*, polarization-mode dispersion, Kerr effect, etc. As a result, the received optical waveform is $r(\cdot) = \rho x(\cdot)$, where $\rho \in (0, 1]$ is the loss factor, depending on the fiber length and the operating wavelength. For simplicity in computations, we assume that $\rho = 1$, which in optical communications is known as back-to-back transmission. It should be mentioned that the BER and the mutual-information figures, discussed in Sec. III, depend on the received optical-signal power. Thus, for a given non-zero transmission length, *i.e.*, with $\rho < 1$, the needed launch power can be computed easily. Examples with $\rho < 1$ are presented in Sec. III.

B. Tukey Signalling

In this section, we describe the “signalling” unit of Fig. 1, which is the central contribution of this paper. For a positive integer n , this unit accepts n complex numbers, $x_0, \dots, x_{n-1} \in \mathbb{C}$, called the transmitted symbols, or simply the symbols, and produces the waveform $x \in \mathbb{C}^{\mathbb{R}}$, given as

$$x(t) = \sum_{d=0}^{n-1} x_d w(t - dT), \quad (1)$$

where $T \in \mathbb{R}^{>0}$ is the inverse of the baud rate, and $w(\cdot)$ is a real-valued signalling waveform. Throughout the paper, n denotes the number of transmitted symbols.

In typical communication systems, $w(\cdot)$ is chosen to be a sinc waveform, a raised-cosine waveform, a root raised-cosine waveform, etc. However, their “ISI patterns” are complicated, *i.e.*, at a given time t when the ISI is non-zero, many, if not all, of the transmitted symbols contribute to the squared-magnitude of $x(t)$. As mentioned in Sec. I, this increases the detection complexity. To avoid this, we require that only a few transmitted symbols should interfere at time t . One way to achieve this is to have $w(\cdot)$ supported over a relatively short time interval. However, this reduction in the “timewidth” of $w(\cdot)$ increases its bandwidth. To tackle this issue, $w(\cdot)$ should have a tapered edge, *i.e.*, it should drop slowly and smoothly toward zero. A familiar function having this behaviour is the

Fourier transform of the raised-cosine function. Note, however, that $w(\cdot)$ must possess this tapering property in the time domain, not in the frequency domain.

We propose the use of the following family of waveforms. For a $\beta \in [0, 1]$, let

$$w_\beta(t) \triangleq \begin{cases} \frac{2}{\sqrt{4-\beta}}, & \text{if } |t| \leq \frac{(1-\beta)}{2}; \\ \frac{1}{\sqrt{4-\beta}} \left(1 - \sin \left(\frac{\pi(2|t|-1)}{2\beta} \right) \right), & \text{if } \left| |t| - \frac{1}{2} \right| \leq \frac{\beta}{2}; \\ 0, & \text{otherwise.} \end{cases} \quad (2)$$

Note that $w_\beta(\cdot)$ has unit energy, i.e., $\int_{-\infty}^{\infty} w_\beta^2(t) dt = 1$, and is supported over a time interval of duration $1+\beta$. This waveform is known in spectrum estimation as the *cosine-tapered window* or the *Tukey window*, named after mathematician and founder of “modern spectrum estimation” [50], John W. Tukey, who suggested them as a combination of *rectangular* and *Hann* windows [51]–[53]. Indeed, $w_0(\cdot)$ and $w_1(\cdot)$ are rectangular and Hann windows, respectively. To avoid introducing a new name for $w_\beta(\cdot)$ as a signalling waveform, we refer to it as a *Tukey waveform*. Fig. 2 shows Tukey waveforms for two different β values.

We set $w(\cdot)$ in (1) to be a dilated Tukey waveform; in particular, $w(t) = w_\beta\left(\frac{t}{T}\right)$. With this choice of $w(\cdot)$, at any time t within the support of $x(\cdot)$, either exactly one or exactly two of the transmitted symbols contribute to $|x(t)|^2$. This property facilitates the recovery of phase information from the induced ISI. Accordingly, we define two types of time intervals, to be used in later sections, as follows. For $k \in \{0, \dots, n-1\}$, $x(t)$ depends only on x_k whenever $|t - kT| \leq \frac{(1-\beta)T}{2}$. Thus, we define the k^{th} ISI-free interval as

$$\mathcal{I}_k \triangleq \left[\left(k - \frac{1-\beta}{2} \right) T, \left(k + \frac{1-\beta}{2} \right) T \right]. \quad (3)$$

Similarly, for $\ell \in \{0, \dots, n-2\}$, $x(t)$ depends on both x_ℓ and $x_{\ell+1}$ whenever $|t - (\ell + \frac{1}{2})T| < \frac{1}{2}\beta T$. Therefore, we define the ℓ^{th} ISI-present interval as

$$\mathcal{Z}_\ell \triangleq \left(\left(\ell + \frac{1-\beta}{2} \right) T, \left(\ell + \frac{1+\beta}{2} \right) T \right). \quad (4)$$

The ISI-free and ISI-present intervals are shown (for $n = 3$) in Fig. 3.

As the waveforms $w_\beta(\cdot)$ are strictly time-limited, they cannot be bandlimited. The Fourier transform of $w_\beta(\cdot)$, denoted as $W_\beta(\cdot)$, is

$$W_\beta(f) \triangleq \begin{cases} \frac{\pi}{2\sqrt{4-\beta}} \text{sinc}\left(\frac{1}{2\beta}\right), & \text{if } f = \frac{\pm 1}{2\beta}; \\ \frac{2}{\sqrt{4-\beta}} \text{sinc}(f) \frac{\cos(\pi\beta f)}{1-(2\beta f)^2}, & \text{otherwise.} \end{cases}$$

Fig. 4 shows $W_\beta(\cdot)$ for two different β values. Tables I and II give the bandwidth of $w_\beta(\cdot)$ which contains, respectively, 95% and 90% of the total energy. For these energy percentiles, the out-of-band signal energy is 12.79 dB and 9.54 dB less than the in-band energy, respectively. One observes that, although not strictly bandlimited, the bandwidth of $w_\beta(\cdot)$ is close to $1/2$

TABLE I
THE BANDWIDTH CONTAINING 95% OF THE $w_\beta(\cdot)$ ENERGY AND ITS OVERHEAD COMPARED TO THE MINIMUM BANDWIDTH FOR NYQUIST SIGNALLING

β	bandwidth	overhead	β	bandwidth	overhead
0.1	1.477	195.4%	0.3	0.788	57.6%
0.5	0.668	33.6%	0.7	0.613	22.6%
0.8	0.592	18.4%	0.9	0.575	15%

TABLE II
THE BANDWIDTH CONTAINING 90% OF THE $w_\beta(\cdot)$ ENERGY AND ITS OVERHEAD COMPARED TO THE MINIMUM BANDWIDTH FOR NYQUIST SIGNALLING

β	bandwidth	overhead	β	bandwidth	overhead
0.1	0.706	41.2%	0.3	0.612	22.4%
0.5	0.56	12%	0.7	0.522	4.4%
0.8	0.505	1%	0.9	0.49	-2%

for large values of β . For example, 95% of the $w_{0.9}(\cdot)$ energy is contained within a spectral band of length 0.575, i.e., a 15% overhead compared to the minimum bandwidth required for Nyquist signalling. Indeed, the numerical simulations in Sec. III support the use of large β values in terms of BER and mutual information.

Note that $w_\beta(\cdot)$ is not orthogonal to its unit-shift replica, i.e., $\int_{-\infty}^{\infty} w_\beta(t)w_\beta(t-1)dt \neq 0$. This lack of orthogonality must be taken into account when computing the average power of the waveform $x(\cdot)$. Luckily, in the case when the symbols are independent and identically distributed (i.i.d.), Theorem 1 shows that this power is indeed given as the mean squared value of the symbol magnitudes.

Theorem 1. For a positive integer m and $P \in \mathbb{R}^{>0}$, let $\lambda_0, \dots, \lambda_{m-1}$ be i.i.d. zero-mean complex random variables such that $\mathbb{E}[|\lambda_0|^2] = P$ and $\text{Var}(|\lambda_0|^2) < \infty$. Furthermore, let

$$\Lambda_m(t) = \sum_{j=0}^{m-1} \lambda_j w_\beta\left(\frac{t}{T} - j\right).$$

Then,

$$\frac{1}{mT} \int_{-\infty}^{\infty} |\Lambda_m(t)|^2 dt \xrightarrow{P} P \quad \text{as } m \rightarrow \infty,$$

i.e., the power of $\Lambda_m(\cdot)$ converges to P in probability.

Proof: See Appendix. ■

We remark that finiteness of $\text{Var}(|\lambda_0|^2)$ is a very mild condition which is true for all finite signal constellations and indeed most of the usual distributions over an infinite range.

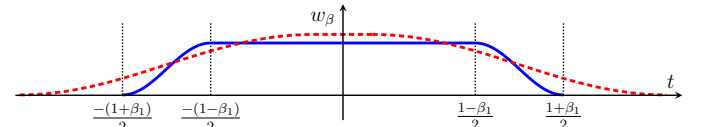


Fig. 2. Tukey waveforms $w_{\beta_1}(\cdot)$ (solid) and $w_{\beta_2}(\cdot)$ (dashed); $\beta_1 < \beta_2$.

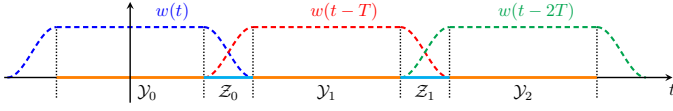


Fig. 3. ISI-free and ISI-present intervals for $n = 3$.

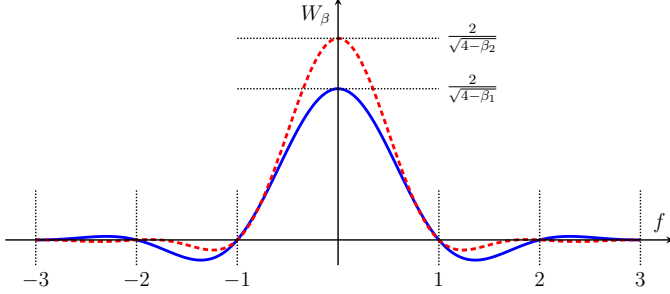


Fig. 4. Fourier transforms of $w_{\beta_1}(\cdot)$ (solid) and $w_{\beta_2}(\cdot)$ (dashed); $\beta_1 < \beta_2$.

C. Photodiode, the Noise Source

The received optical waveform, $r(\cdot)$, is converted to an electrical signal by a photodiode. In our model, the photodiode is the only source of noise. The photodiode has a gain which, for simplicity, is assumed to be unity in this section. However, the actual gain is taken into account in the numerical simulations presented in Sec. III. The output of the photodiode is a real-valued waveform $s(\cdot)$, such that

$$s(t) = |r(t)|^2 + |r(t)|n_{\text{sh}}(t) + n_{\text{th}}(t), \quad (5)$$

where $n_{\text{sh}}(\cdot)$ and $n_{\text{th}}(\cdot)$ are independent zero-mean white Gaussian random processes with constant two-sided power spectral densities (PSDs) σ_{sh}^2 and σ_{th}^2 , respectively. The $|r(t)|n_{\text{sh}}(t)$ and $n_{\text{th}}(t)$ terms are known, respectively, as shot noise and thermal noise [8]. It should be mentioned that photodiodes have additional practical deficiencies, such as, e.g., dark current. However, we assume that such effects contribute negligibly compared to the noise terms in (5).

D. Integrate & Dump

In this section, we discuss the integrate-and-dump unit in Fig 1. As noted in Sec. II-B, at any time t within the support of $x(\cdot)$, either exactly one or exactly two of the transmitted symbols contribute to $|x(t)|^2$. The integrate-and-dump unit integrates its input waveform over each \mathcal{Y}_k and \mathcal{Z}_{ℓ} interval, producing y_k and z_{ℓ} , respectively, where $k \in \{0, \dots, n-1\}$ and $\ell \in \{0, \dots, n-2\}$. More precisely,

$$y_k \triangleq \int_{\mathcal{Y}_k} s(t)dt, \quad (6)$$

and

$$z_{\ell} \triangleq \int_{\mathcal{Z}_{\ell}} s(t)dt. \quad (7)$$

We expand (6) as follows. Let $\alpha \triangleq \frac{2}{\sqrt{4-\beta}}$; then, by using $r(\cdot) = x(\cdot)$ (see Sec. II-A), we get

$$y_k = \alpha^2(1-\beta)T|x_k|^2 + \alpha|x_k|n_k + m_k, \quad (8)$$

where

$$n_k \triangleq \int_{\mathcal{Y}_k} n_{\text{sh}}(t)dt \sim \mathcal{N}(0, \sigma_{\text{sh}}^2(1-\beta)T),$$

and

$$m_k \triangleq \int_{\mathcal{Y}_k} n_{\text{th}}(t)dt \sim \mathcal{N}(0, \sigma_{\text{th}}^2(1-\beta)T).$$

Note that $\mathbb{E}[n_k n_{k'}] = \mathbb{E}[m_k m_{k'}] = 0$, for any $k' \neq k$, where $k' \in \{0, \dots, n-1\}$.

We expand (7) as follows. Let $\psi : \mathbb{C}^2 \rightarrow \mathbb{R}$ be defined as

$$\psi(v, w) = \frac{1}{4}|v + w|^2 + \frac{1}{8}|v - w|^2,$$

for any v and $w \in \mathbb{C}$. Then, (7) can be simplified as

$$z_{\ell} = \alpha^2 \beta T \psi(x_{\ell}, x_{\ell+1}) + \alpha \sqrt{\psi(x_{\ell}, x_{\ell+1})} p_{\ell} + q_{\ell}, \quad (9)$$

where $p_{\ell} \sim \mathcal{N}(0, \beta T \sigma_{\text{sh}}^2)$, and $q_{\ell} \sim \mathcal{N}(0, \beta T \sigma_{\text{th}}^2)$. Similarly, $\mathbb{E}[p_{\ell} p_{\ell'}] = \mathbb{E}[q_{\ell} q_{\ell'}] = 0$, for any $\ell' \neq \ell$. Note that for any k and $k' \in \{0, \dots, n-1\}$ and for any ℓ and $\ell' \in \{0, \dots, n-2\}$, the four random variables $n_k, m_{k'}, p_{\ell}$, and $q_{\ell'}$ are mutually independent.

E. Equivalence Classes

In this section, we describe the first transmitter block in Fig. 1, i.e., choice of class representative. Let $\Upsilon : \mathbb{C}^n \rightarrow \mathbb{R}^n \times \mathbb{R}^{n-1}$ denote the function that maps a vector $\mathbf{x} = (x_0, \dots, x_{n-1}) \in \mathbb{C}^n$ at the input of the signalling block to the corresponding output of the integrate-and-dump block in the absence of noise and loss (i.e., in a back-to-back configuration with $L = 0$), as shown in Fig. 5. Specifically, if $x(t) = \sum_{d=0}^{n-1} x_d w(t-dT)$ then $\Upsilon(\mathbf{x}) = (\mathbf{y}, \mathbf{z})$, where $\mathbf{y} \in \mathbb{R}^n$ is such that

$$\mathbf{y}[k] = \int_{\mathcal{Y}_k} |x(t)|^2 dt,$$

for $k \in \{0, \dots, n-1\}$, and $\mathbf{z} \in \mathbb{R}^{n-1}$ is such that

$$\mathbf{z}[\ell] = \int_{\mathcal{Z}_{\ell}} |x(t)|^2 dt,$$

for $\ell \in \{0, \dots, n-2\}$.

We define an equivalence relation on \mathbb{C}^n as follows. Two vectors \mathbf{x} and $\tilde{\mathbf{x}} \in \mathbb{C}^n$ are said to be *square-law identical*, denoted $\mathbf{x} \equiv \tilde{\mathbf{x}}$, if and only if $\Upsilon(\mathbf{x}) = \Upsilon(\tilde{\mathbf{x}})$. If \mathbf{x} and $\tilde{\mathbf{x}}$ are not square-law identical, they are said to be *square-law distinct*, denoted $\mathbf{x} \not\equiv \tilde{\mathbf{x}}$. Since the relation \equiv is indeed an equivalence relation, it partitions \mathbb{C}^n into disjoint equivalence classes.

Example 1. Let $\mathbf{x} = (1, i, 1, -1)$ and $\tilde{\mathbf{x}} = (1, i, -1, 1)$. For both of these vectors we have $\Upsilon(\mathbf{x}) = \Upsilon(\tilde{\mathbf{x}}) = (\mathbf{y}, \mathbf{z})$ where $\mathbf{y} = \alpha^2(1-\beta)T(1, 1, 1, 1)$ and $\mathbf{z} = \alpha^2 \beta T(\frac{3}{4}, \frac{3}{4}, \frac{1}{2})$. Therefore, $\mathbf{x} \equiv \tilde{\mathbf{x}}$, i.e., \mathbf{x} and $\tilde{\mathbf{x}}$ are square-law identical. However, for $\hat{\mathbf{x}} = (1, -1, 1, i)$ we have $\Upsilon(\hat{\mathbf{x}}) = (\hat{\mathbf{y}}, \hat{\mathbf{z}})$ where $\hat{\mathbf{y}} = \mathbf{y}$, but $\hat{\mathbf{z}} = \alpha^2 \beta T(\frac{1}{2}, \frac{1}{2}, \frac{3}{4}) \neq \mathbf{z}$; therefore, $\mathbf{x} \not\equiv \hat{\mathbf{x}}$.

For any positive integer M , let \mathcal{S} be a set of cardinality M , whose elements are complex-valued vectors of length n , called *symbol blocks*, which are square-law distinct. In other words, $\mathcal{S} = \{\mathbf{x}_1, \dots, \mathbf{x}_M\} \subset \mathbb{C}^n$ such that $\mathbf{x}_k \not\equiv \mathbf{x}_{\ell}$ if $k \neq \ell$.

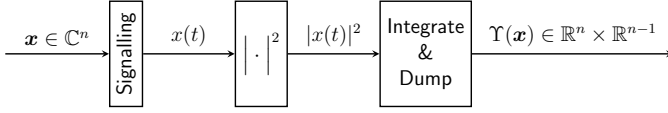


Fig. 5. The Υ function maps the input of the signalling block to the corresponding output of the integrate-and-dump block in the absence of noise. The noisy photodiode of Fig. 1 has been replaced with an ideal $|\cdot|^2$ block.

Then, the class-representative unit outputs the symbol block \mathbf{x}_k if its input is $k \in \{1, \dots, M\}$. Note that the entries of symbol blocks are in fact the transmitted symbols, i.e., the set \mathcal{S} forms a signal constellation in n complex dimensions ($2n$ real dimensions). Furthermore, note that the spectral efficiency of this communication scheme cannot exceed $\frac{1}{n} \log_2(M)$ bit/sec/Hz.

F. Maximum-Likelihood Block Detection

The last block of Fig. 1 is the detector. In practice, the choice of detection rule and its algorithm will depend on hardware limitations and performance requirements. Through out this paper, maximum-likelihood (ML) block detection is chosen as the detection rule. In other words, if $\mathbf{y} = (y_0, \dots, y_{n-1})$ and $\mathbf{z} = (z_0, \dots, z_{n-2})$ are the buffered outputs of the integrate-and-dump unit, the detector chooses $\hat{k} \in \{1, \dots, M\}$ as the transmitted index if and only if

$$\hat{k} = \arg \max_{d \in \{1, \dots, M\}} f(\mathbf{y}, \mathbf{z} | \mathbf{x}_d).$$

For any $k \in \{0, \dots, n-1\}$, (8) implies that, given x_k ,

$$y_k \sim \mathcal{N}\left(\alpha^2(1-\beta)T|x_k|^2, (1-\beta)T(\alpha^2|x_k|^2\sigma_{\text{sh}}^2 + \sigma_{\text{th}}^2)\right). \quad (10)$$

Furthermore, for any $\ell \in \{0, \dots, n-2\}$, (9) implies that, given x_ℓ and $x_{\ell+1}$,

$$z_\ell \sim \mathcal{N}\left(\alpha^2\beta T\psi(x_\ell, x_{\ell+1}), \beta T(\alpha^2\psi(x_\ell, x_{\ell+1})\sigma_{\text{sh}}^2 + \sigma_{\text{th}}^2)\right). \quad (11)$$

Thus,

$$\begin{aligned} f(\mathbf{y}, \mathbf{z} | \mathbf{x}_d) &= f(\mathbf{y} | \mathbf{x}_d) f(\mathbf{z} | \mathbf{x}_d) \\ &= \prod_{k=0}^{n-1} f(y_k | \mathbf{x}_d[k]) \prod_{\ell=0}^{n-2} f(z_\ell | \mathbf{x}_d[\ell], \mathbf{x}_d[\ell+1]), \end{aligned} \quad (12)$$

where $f(y_k | \mathbf{x}_d[k])$ and $f(z_\ell | \mathbf{x}_d[\ell], \mathbf{x}_d[\ell+1])$ can be computed from (10) and (11), respectively. Fig. 6 is the factor-graph representation [54] of (12). Note that the variances of y_k and z_ℓ , given in (10) and (11), are functions of the transmitted symbols; therefore, minimum Euclidean-distance detection is *not* equivalent to ML block detection.

III. NUMERICAL SIMULATION

In this section, the communication scheme proposed in Sec. II is verified by numerical simulations.

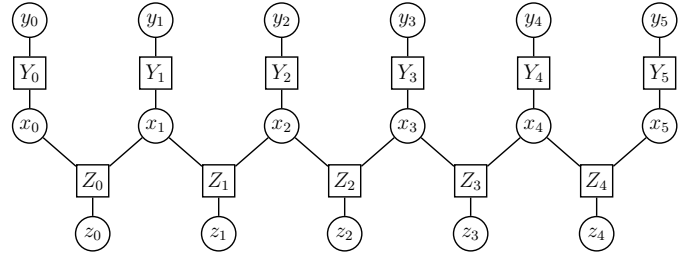


Fig. 6. The factor graph of the ML block detection for $n = 6$. For $k \in \{0, \dots, 5\}$, the Y_k factor node represents $f(y_k | x_k)$. Similarly, for $\ell \in \{0, \dots, 4\}$, the Z_ℓ factor node represents $f(z_\ell | x_\ell, x_{\ell+1})$.

TABLE III
PARAMETER VALUES USED IN THE NUMERICAL SIMULATION

Parameter	Value	Typical Range (InGaAs APD)
Temperature (T_k)	300 K	
Load Resistance (R_L)	15 Ω	
APD Gain (M_{APD})	20	10 – 40
Enhanced Responsivity ($M_{\text{APD}} R_{\text{APD}}$)	10 mA/mW	5 – 20
k -factor (k_{APD})	0.6	0.5 – 0.7
Excess Noise Factor (F)	12.78	a function of M_{APD} and k_{APD}

A. The Photodiode

We assume the use of an InGaAs avalanche photodiode (APD), as among different types of APDs, these have high bandwidth. In this case, the two-sided PSD of the thermal noise, $n_{\text{th}}(\cdot)$, is [8]

$$\sigma_{\text{th}}^2 = \frac{2kT_k}{R_L},$$

where k is the Boltzmann constant, T_k is the temperature, and R_L is the external load resistance. Furthermore, for the received optical complex-valued waveform $r(\cdot)$, the shot noise is $|r(t)|n_{\text{sh}}(t)$, where the two-sided PSD of $n_{\text{sh}}(\cdot)$ is

$$\sigma_{\text{sh}}^2 = eM_{\text{APD}}^2FR_{\text{APD}},$$

where e is the unit charge, M_{APD} is the APD gain, F is the excess noise factor, and R_{APD} is the responsivity of APD. Table III gives the values for these parameters used in simulations.

B. The Transmitted Symbols

The transmitted symbols are chosen from a finite constellation, \mathcal{K} , three of which are shown in Fig. 7. Indeed, $\mathcal{S} \subset \mathcal{K}^n$, and since the symbol blocks must be square-law distinct, there is a loss in the maximum achievable rate in the proposed scheme, compared to its coherent-detection counterpart. Table IV provides the number of equivalent classes of each possible size for different values of n , and for 2-ring/4-ary phase constellation (see Fig. 7b). For example, for $n = 4$ there are 432 equivalence classes, among which 192 have size 8. As there are $|\mathcal{K}|^n = 8^4$ possible vectors of length 4 over \mathcal{K} , the lost rate is $\frac{1}{4} \log_2 \left(\frac{8^4}{432} \right) = 0.94$ bits per symbol. Table IV shows that the larger is n , the smaller is the rate loss. However, this reduction in rate loss comes with a higher

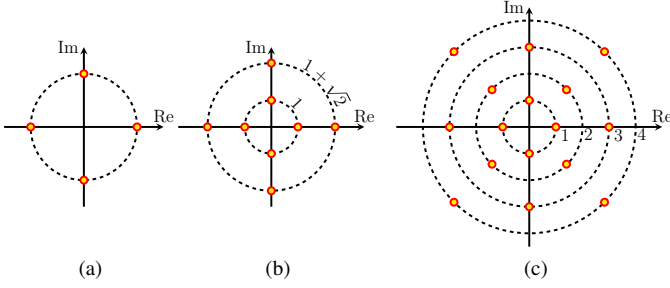


Fig. 7. Three choices for \mathcal{K} , the constellation from which the transmitted symbols come: (a) 4-PSK (phase shift keying), (b) 2-ring/4-ary phase, and (c) 4 ring/4-ary phase constellations. The ratio of the outer-ring radius to the inner one in (b) is $1 + \sqrt{2}$. In (c), the rings are equi-spaced.

TABLE IV
NUMBER OF CLASSES FOR EACH CLASS SIZE FOR 2-RING/4-ARY PHASE CONSTELLATION

class size \ n	3	4	5	6	7
4	32	128	512	2048	8192
8	32	192	1024	5120	24576
16	8	96	768	5120	30720
32		16	256	2560	20480
64			32	640	7680
128				64	1536
256					128
Total	72	432	2592	15552	93312
Rate loss (bit/sym)	0.94	0.81	0.73	0.68	0.64
$\frac{1}{n} \log_2 \left(\frac{8^n}{\text{Total}} \right)$					

detection complexity. Specifically, the number of equivalence classes grows exponentially with n , which itself increases the complexity of the ML block decoder.

It should be noted that a relatively small n suffices to achieve a practical target BER. This is because the transmission scheme is usually the inner-most layer of a larger communication system, which typically also employs an outer error-correcting code.

C. Mutual Information

Fig. 8 shows the achievable rate per symbol in different scenarios, plotted against the received optical power (ROP), computed by a Monte Carlo method. To compute the spectral efficiency in bit/sec/Hz one must choose the measure of bandwidth, e.g., 90% in-band energy, 95% in-band energy, etc., that suits the application restrictions. The spectral efficiency can then be computed readily.

In Figs. 8(a)–8(e), the transmitted symbol block is chosen independently and uniformly among all symbol blocks, i.e., class representatives. In Fig. 8(f), instead of square-law distinct symbol blocks, all possible vectors of \mathcal{K}^n have been chosen with uniform distribution. As equivalence classes have different cardinalities (see Table IV), a uniform distribution over \mathcal{K}^n induces a non-uniform distribution over equivalence-class representatives, giving rise to a huge loss in the achievable rate compared to Figs. 8(a)–8(e). Thus it is important that the transmitted symbol blocks are chosen to be square-law distinct.

As shown in Figs. 8(a)–8(d), the value of β affects the minimum required power to achieve a target data rate, for a

fixed constellation \mathcal{K} . We find that $\beta = 0.9$ either outperforms other choices of β at close-to-saturation data rates, or the loss is negligible compared to other values of β .

Inspired by [55], Fig. 8(e) shows the mutual information for different constellations and with different values of n , all with $\beta = 0.9$. This figure can be interpreted in two different ways, as follows. First, by fixing the ROP at a constant value, we can achieve a higher data rate by choosing a larger constellation. For example, at the ROP of -16 dBm and with $n = 3$, a data rate of 2 bit/sym is achievable with the 2-ring/4-ary phase constellation, while a data rate of 2.7 bit/sym is achievable with the 4-ring/4-ary phase constellation. Secondly, by selecting a larger \mathcal{K} , a target data rate is achievable at a smaller ROP. For example, the data rate of 2 bit/sym is achievable by the 2-ring/4-ary phase constellation with $n = 4$ at an ROP $\simeq -19$ dBm, while by using the 4-ring/4-ary phase constellation, with $n = 3$ and a channel code of rate $\simeq 0.7$, the same data rate is achievable at the ROP of -24 dBm, i.e., with approximately a 5 dB gain. Note that the number of equivalence classes in the former is 432, while in the latter it is 400; therefore, their ML block-detection complexities are roughly the same.

As discussed earlier in this section, for a fixed constellation \mathcal{K} , the achievable rate will increase with increasing n . This fact can be seen from Fig. 8(e). For example, while the maximum achievable rate for 4-ring/4-ary phase constellation is 2.88 bit/sym for $n = 3$, the maximum achievable rate is 2.99 and 3.08 bit/sym for $n = 4$ and $n = 5$, respectively. If one chooses the 90% in-band energy as the criterion for defining the bandwidth, then the spectral efficiencies for $n = 3$, $n = 4$, and $n = 5$ is, respectively, 2.94, 3.05, and 3.14 bit/sec/Hz. Note that the maximum rate for this constellation is 4 bit/sec/Hz under coherent detection; therefore, in the last two cases, i.e., $n = 4$ and $n = 5$, the rate is within the bounds given in [21], [22]. Furthermore, although the spectral efficiency for $n = 3$ is below the rate lower-bound i.e., 3 bit/sec/Hz, the gap is small, i.e., about 2%. By the same bandwidth definition, the maximum spectral efficiency for other constellations in Fig. 8(e) are all within one bit/sec/Hz of coherent detection. However, if one chooses the 95% in-band energy as the criterion for specifying the bandwidth then, except the 4-PSK constellation, the spectral-efficiency gap with coherent detection is greater than one bit/sec/Hz. For example, the maximum spectral efficiency for 2-ring/4-ary phase constellation with $n = 4$ becomes 1.9 bit/sec/Hz which is 5% smaller than the lower bound, i.e., 2 bit/sec/Hz.

D. Bit Error Rate

Fig. 9 shows the bit error rate of the proposed scheme in a back-to-back ($L = 0$) configuration, for several \mathcal{K} , β , and n . In each scenario, M is chosen to be an integer power of 2. For example, while there are 432 equivalence classes for the 2-ring/4-ary phase constellation with $n = 4$, only $M = 2^8$ of them are chosen as the symbol blocks, i.e., members of \mathcal{S} . The length $\log_2(M)$ binary label associated with each of the M symbols was chosen randomly, i.e., no particular labelling algorithm, e.g., Gray code, is being used.

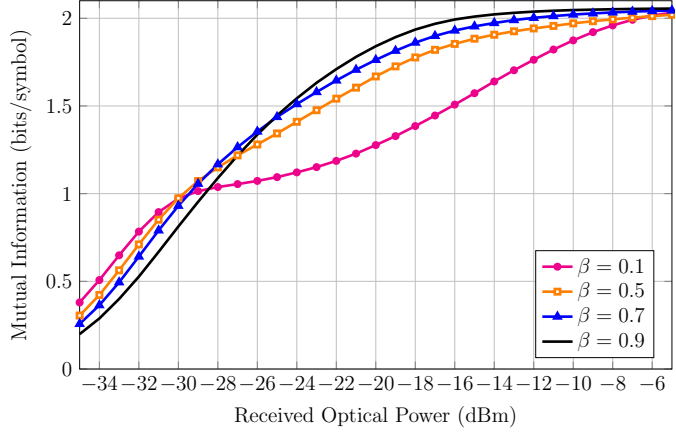
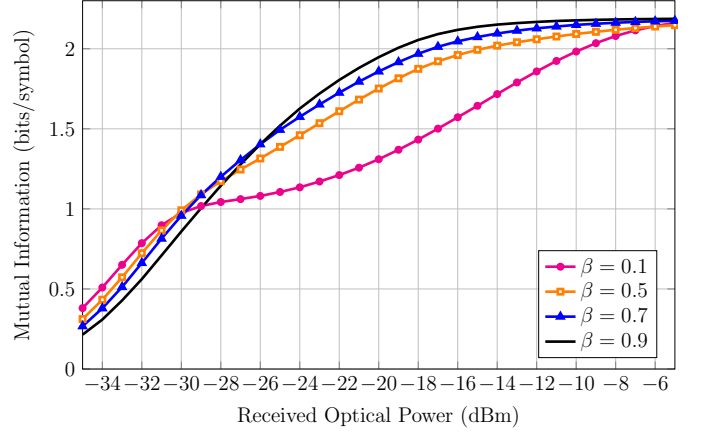
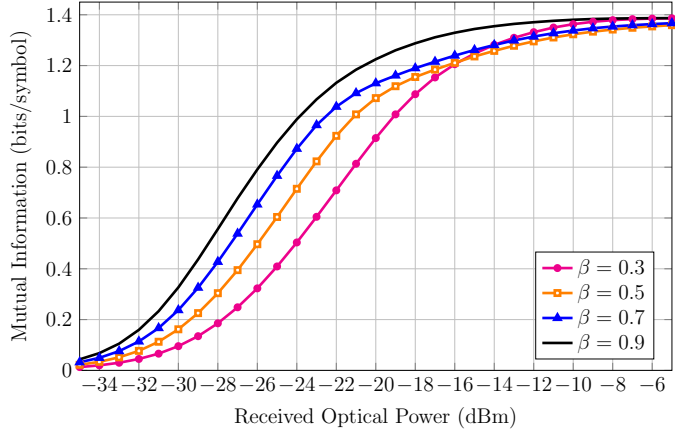
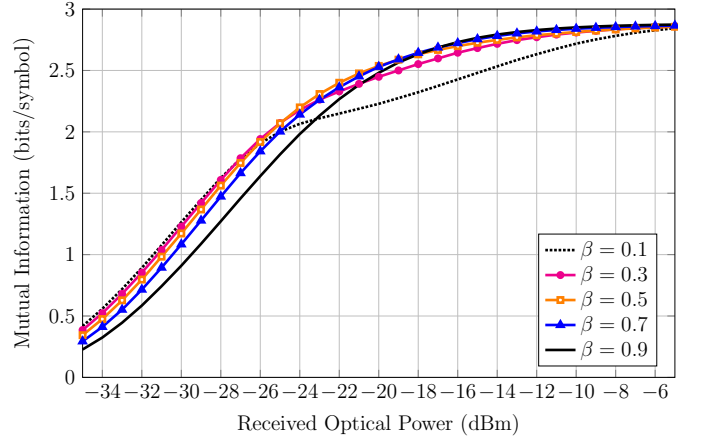
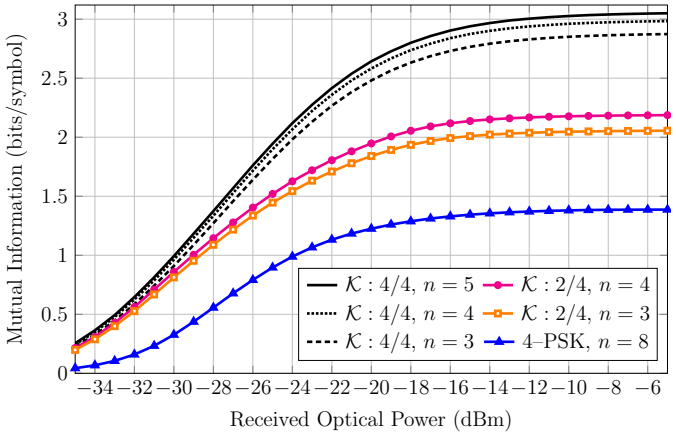
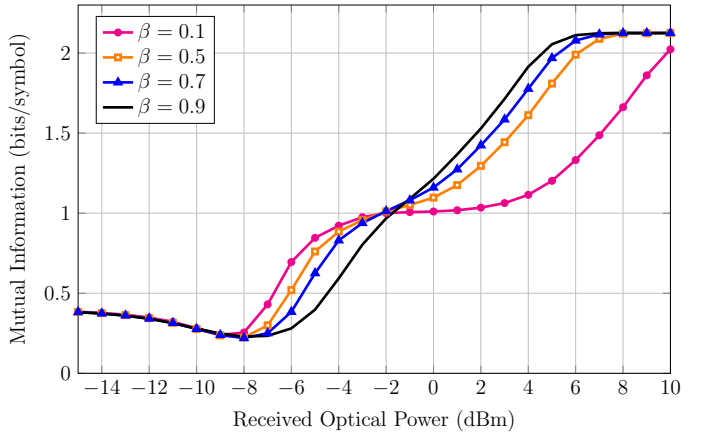
(a) \mathcal{K} : 2-ring/4-ary phase constellation, $n = 3$ (b) \mathcal{K} : 2-ring/4-ary phase constellation, $n = 4$ (c) \mathcal{K} : 4-PSK, $n = 8$ (d) \mathcal{K} : 4-ring/4-ary phase constellation, $n = 3$ (e) Uniform input distribution over all equivalence classes, $\beta = 0.9$ (f) Uniform input distribution over \mathcal{K}^4 , \mathcal{K} : 2-ring/4-ary phase constellation

Fig. 8. Mutual information in different scenarios. In (a)–(e) the input distribution is uniform over all equivalence classes, while in (f) the input distribution is uniform over \mathcal{K}^4 , where \mathcal{K} is the 2-ring/4-ary phase constellation. In part (e), $\mathcal{K} : a/b$ means that \mathcal{K} is an a -ring/ b -ary phase constellation.

As shown in Fig. 9(a), for the 2-ring/4-ary phase constellation, the BER decreases when increasing β from 0.3 to 0.99. It might be perceived from this figure that a larger value of β results in a better BER performance; therefore, the best BER performance is achieved for the maximum possible value for β , *i.e.*, unity. However, Fig. 9(b) refutes this claim. As shown in this figure, for close-to-unity values of β , a small β increment results in a significant performance loss, in terms of BER. In the extreme case, *i.e.*, $\beta = 1$, there is no ISI-free sample, and the n complex-valued transmitted symbols must be detected from the $n - 1$ real-valued ISI-present received samples. Thus, there is a significant performance loss, both in terms of BER and the maximum achievable rate.

The BER performance under 4-PSK and 4-ring/4-ary phase constellations are shown in Fig. 9(c) and Fig. 9(d), respectively. In both cases, the performance is improved by increasing β from 0.1 toward 0.9.

Despite the fact that $\beta = 0.99$ has the best BER performance in Fig. 9(a) for the 2-ring/4-ary phase constellation, because of the discussed high sensitivity of performance to the value of β for $\beta > 0.99$, $\beta = 0.9$ is used to compare the BER of different constellations in Fig. 9(e). For the purpose of fairness, the horizontal axis is normalized to information rate. Similar to a typical communication over an additive white Gaussian noise (AWGN) channel, for a fixed noise power and at high signal powers, using a larger constellation results in a higher BER; however, at low ROPs, the BER performance is a complicated function of the received power.

The choice of constellation \mathcal{K} has a big impact on the performance of the proposed scheme. For example, while 16-QAM (quadrature amplitude modulation) is a typical constellation in communication over AWGN channels, it has very poor performance in the proposed scheme, as shown in Fig. 9(f).

The BER performance for a nonzero fiber length, *i.e.*, $\rho < 1$, for 2-ring/4-ary and 4-ring/4-ary phase constellations are shown in Figs. 10(a) and 10(b), respectively. The split-step Fourier method [56] was used to approximate wave propagation through a 10 km standard single-mode fiber (SSMF) at an operating wavelength of $\lambda = 1550$ nm. One observes that, by using a 4-ring/4-ary phase constellation with 256 symbol blocks of length $n = 3$ and $\beta = 0.9$, a BER of 10^{-3} is resulted at a -10 dBm launch power. As the power loss of SSMF at this wavelength is about $0.2 \text{ dB} \cdot \text{km}^{-1}$; a -10 dBm launch power results a -12 dBm ROP. Note that this agrees with Fig. 9(d), *i.e.*, a BER of 10^{-3} resulted from same system parameters at a -12 dBm ROP. At higher launch powers, however, there is a discrepancy between the figures, resulting from uncompensated nonlinear fiber impairments. To achieve a high data rate, one may operate in the low-to-moderate launch-power regime—where fiber nonlinearity is not a critical factor—by choosing high-order constellations. If high detection complexity rules high-order constellations out then one might use low-order constellations and operate at high launch powers by precompensating not only the chromatic dispersion but also the fiber nonlinear impairments at the transmitter. However, such nonlinear precompensation, which might be implemented by a form of digital back-propagation [57], will itself incur significant implementation complexity.

E. Power

If the transmitted symbols are i.i.d., Theorem 1 guarantees that the average power of the transmitted waveform is equal, in probability, to the variance of those symbols. On the other hand, in Sec. III-C it was noted that uniform selection of symbol blocks from the entire \mathcal{K}^n results in a significant loss in achievable rate, and therefore must be avoided. Constraining symbol blocks to be square-law distinct makes the transmitted symbols dependent, and thus Theorem 1 does not apply. However, in the numerical simulations it turned out that the average power of the transmitted waveform is indeed equal to \mathcal{P}_S in all cases studied, where $\mathcal{P}_S \triangleq \frac{1}{Mn} \sum_{j=1}^M \|\mathbf{x}_j\|^2$ is the average power of \mathcal{S} and where $\|\cdot\|$ denotes the L^2 -norm.

F. Comparison With Other Schemes

Due to differences in channel models, particularly the idealization of optical fibers, a fair comparison of the proposed scheme with other existing schemes is difficult. For example, while we have assumed that there are no optical amplifiers, and, as a result, no ASE noise in the channel, many papers in the literature use erbium-doped fiber amplifiers, which are primary sources of ASE noise.

Although not exactly fair, to make a comparison, let us assume the proposed scheme is used to transmit data over a span of 10 km of SSMF. The resulting power loss at 1550 nm is 2 dB. Factoring in an additional 5 dB loss due, *e.g.*, to connector losses and code operation at some gap to the Shannon limit, let us assume the launch power is 7 dB larger than the received power. In this case, from Fig. 8(e) we see that an information rate of 2 bits per symbol can be achieved with the proposed scheme, by using the 4-ring/4-ary phase constellation with $n = 4$ and a channel code of rate $2/3$, at a launch power of -17.5 dBm.

On the other hand, using a Kramers–Kronig receiver, the authors of [26] achieve a data rate of 4 bits per symbol at a launch power of 2 dBm. Under the rule of thumb that each additional 3 dB launch power yields an extra bit per symbol in AWGN channels, the scheme of [26] would be able to achieve a rate of 2 bits per symbol at a launch power of about -4 dBm. However, as noted, the channel model of [26] is quite different.

IV. COMPLEXITY

In this section we discuss the implementation complexity of direct detection under Tukey signalling. Note that the proposed scheme aims to achieve spectral efficiencies close to those of a coherent detector. Therefore—instead of comparing with simple IM/DD schemes whose rates are roughly half the data rate under coherent detection—the complexity of the proposed scheme must be compared with schemes that modulate complex-valued waveforms, *e.g.*, coherent and Kramers–Kronig transceivers.

Fig. 11 shows simple examples of analog and digital integrate-and-dump circuits. Other circuit topologies, designed specifically for high baud rate fiber-optic communications, are well investigated [58]. In order to integrate the output of the photodiode over the ISI-free and ISI-present intervals,

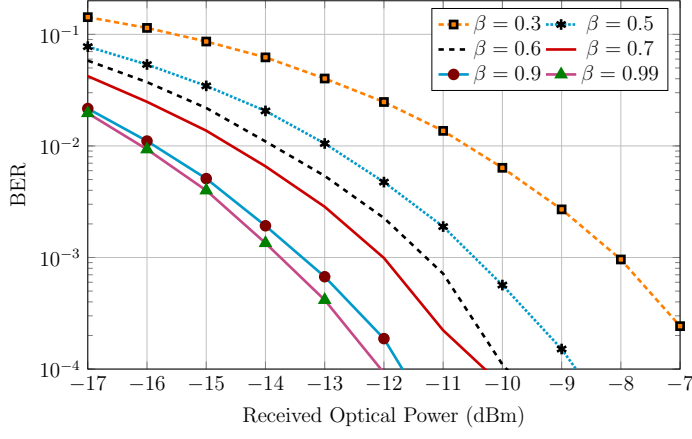
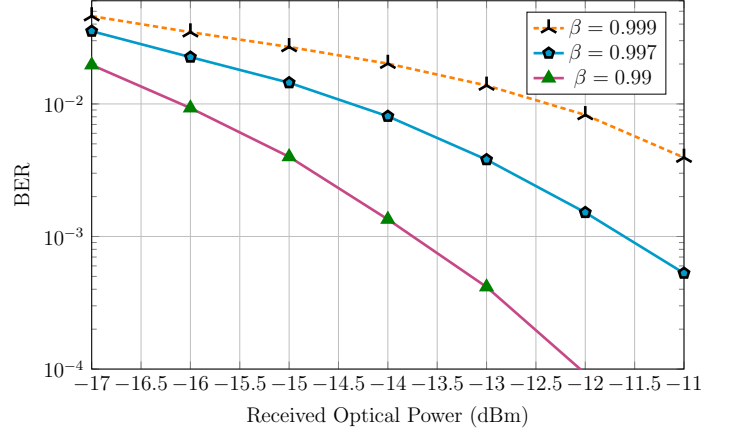
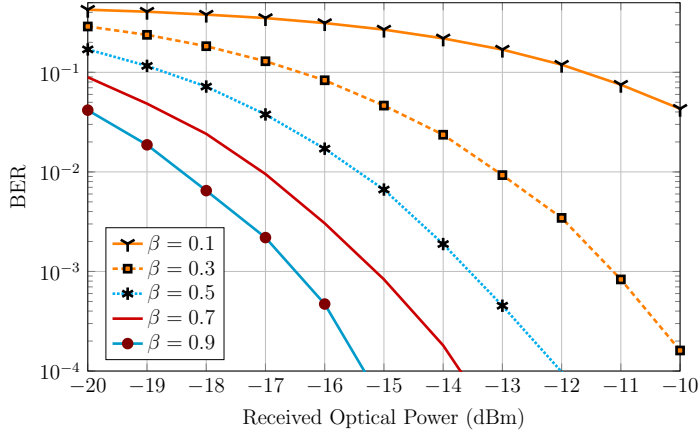
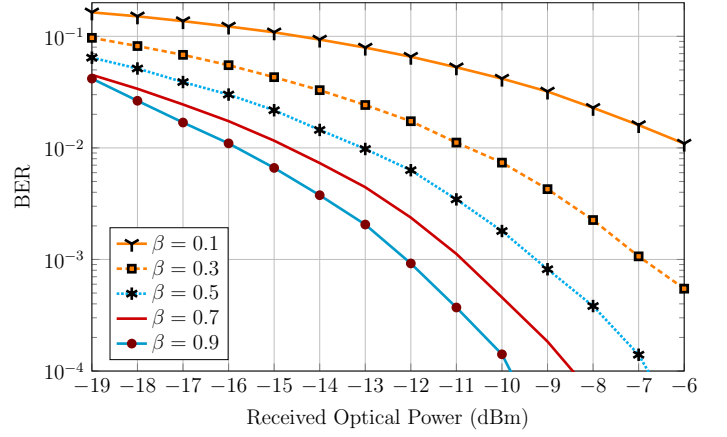
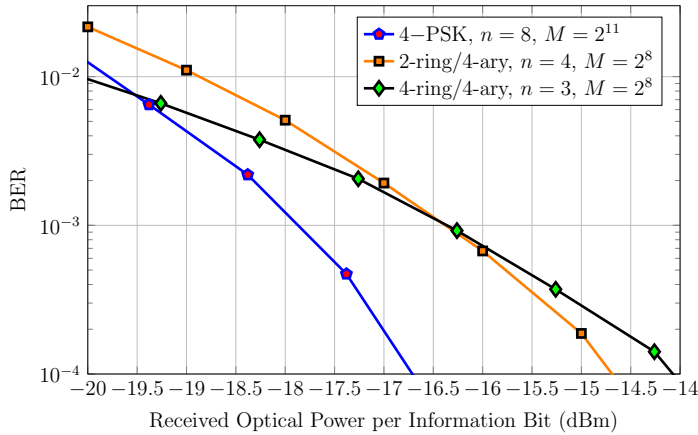
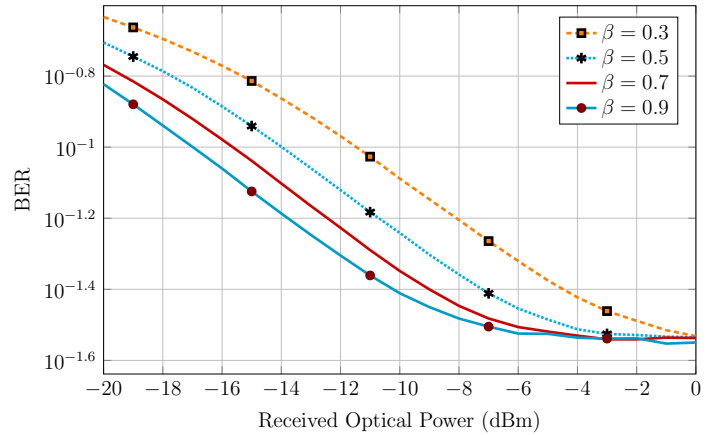
(a) \mathcal{K} : 2-ring/4-ary phase constellation, $n = 4$, $M = 2^8$ (b) \mathcal{K} : 2-ring/4-ary phase constellation, $n = 4$, $M = 2^8$ (c) \mathcal{K} : 4-PSK, $n = 8$, $M = 2^{11}$ (d) \mathcal{K} : 4-ring/4-ary phase constellation, $n = 3$, $M = 2^8$ (e) Different constellations with $\beta = 0.9$ (f) \mathcal{K} : 16-QAM, $n = 3$, $M = 2^8$

Fig. 9. Bit error rate in back-to-back transmission in different scenarios. Part (f) suggests that the conventional 16-QAM constellation does not have a good performance under the proposed communication scheme.

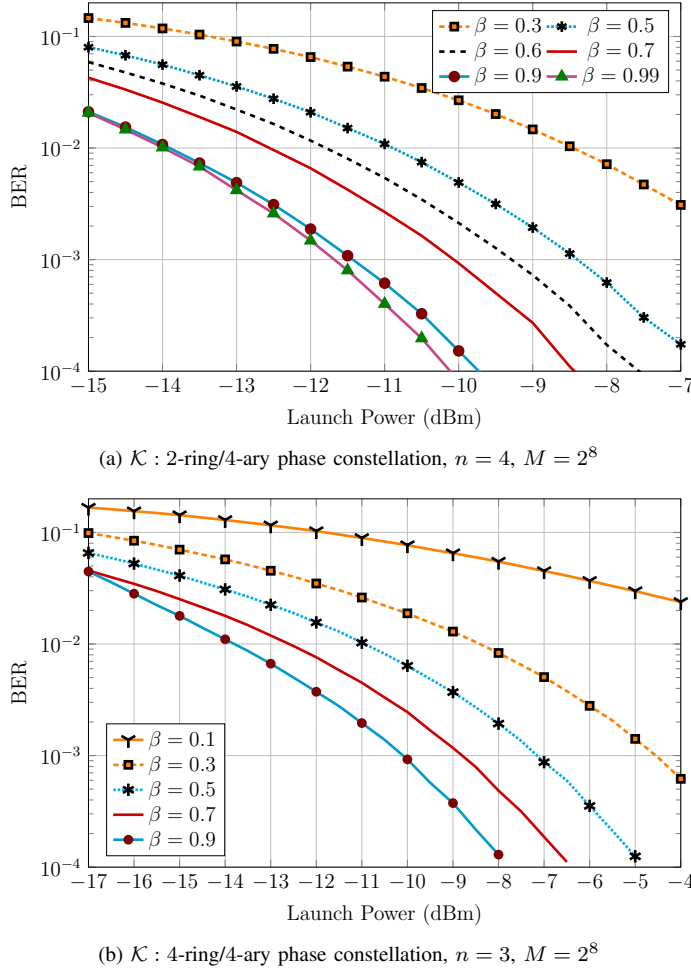


Fig. 10. BER performance of the proposed scheme for a 10 km standard single-mode fiber at the 1550 nm operating wavelength. The propagation through the optical fiber is approximated by the split-step Fourier method.

a clock with a duty cycle of β and its negation is needed. Two analog-to-digital converters (ADCs), each operating at the baud rate, are needed to convert $s(\cdot)$ into discrete-time output samples, *i.e.*, y_k 's and z_ℓ 's, where $k \in \{0, \dots, n-1\}$ and $\ell \in \{0, \dots, n-2\}$. This number of ADCs is exactly the same required in coherent detection, as shown in Fig. 12. The spectrum-broadening operations in typical Kramers–Kronig receivers necessitates even higher conversion rates, *e.g.*, six times the baud rate. However, there are some schemes that allow sampling at twice the baud rate, but under some assumptions, *e.g.*, high carrier-to-signal power ratio [59], [60].

Similar to coherent and Kramers–Kronig transceiver schemes, both the in-phase and the quadrature components of the transmitted waveform are modulated. In other words, the electric field itself (and not just the field intensity) is modulated. Therefore, an *IQ modulator* with two ADCs, one for the in-phase and one for the quadrature components, are needed at the transmitter.

Equivalence class representatives for a particular constellation \mathcal{K} and block length n can be pre-computed and stored in a look-up table. Thus there is no operational complexity related to determining the set \mathcal{S} .

The naive scheme for ML block detection searches over

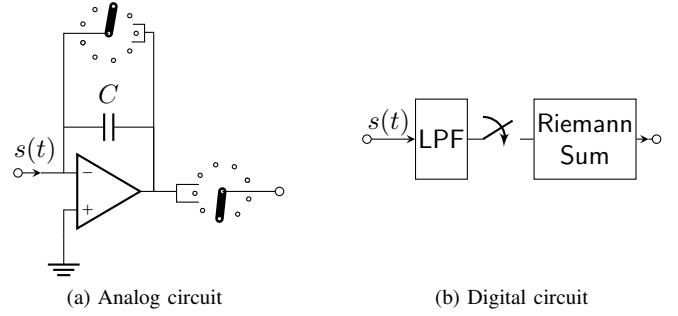


Fig. 11. Simple integrate & dump circuits, LPF: low-pass filter. While the forked wiring above the capacitor in (a) short-circuits the capacitor at the start of each integration interval, the one in front of the op-amp samples the integrator output. Improved integrate-and-dump schemes can be found in [58].

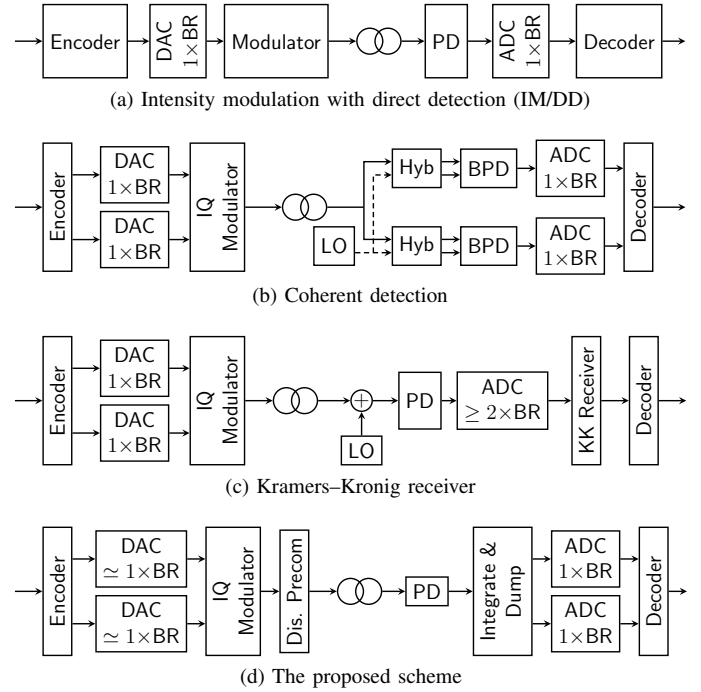


Fig. 12. Abstract block diagrams for four different transceiver schemes. BR: baud rate, DAC: digital to analog converter, ADC: analog to digital converter, PD: photodiode, BPD: balanced photo detector, LO: local oscillator, Hyb: hybrid, Dis. Precom: dispersion precompensation. The numbers below DACs and ADCs show the conversion speed compared to the baud rate. In the Kramers–Kronig receiver, instead of the receiver optical front-end, the tone can be injected to the signal at the transmitter back-end. Except the IM/DD scheme, the modulated waveform is complex valued in the other ones.

all $|\mathcal{S}|$ transmitted blocks to maximize the likelihood score. Therefore, its complexity is $\mathcal{O}(2^{nr_{\max}})$, where r_{\max} is the maximum achievable rate with \mathcal{S} . As mentioned in Sec. III-B, a small n suffices to achieve a target BER; thus, the complexity of the ML block detection is a relatively small fixed constant. It may be possible to reduce this complexity, for example, via a trellis-search algorithm, but we leave the investigation of this for future work.

V. DISCUSSION

As well stated by Tukey, “the test of a good procedure is how well it works, not how well it is understood” [61]. So far

the proposed scheme has been tested only with computer simulations. It would be interesting to investigate its performance in a practical experiment.

Throughout this paper, we have assumed an unamplified optical link and therefore no ASE noise in the system. It would be interesting to investigate the performance of the proposed scheme in the presence of ASE noise.

We have used maximum-likelihood block detection to detect the transmitted symbol block. It would be interesting to investigate other detection strategies. For example, we have assumed that blocks are transmitted without guard time, which means that the last symbol of one block interferes with the first symbol of the next block. While our block detection rule ignores the signal received during these intervals of overlap, a sequence-oriented detection algorithm could potentially exploit them.

As noted in Sec. II-F, unlike AWGN channels, Euclidean distance is not an appropriate metric for detecting the transmitted symbol block. It would be interesting to derive an appropriate metric for the proposed scheme. In addition to giving an insight on detection, such a metric might simplify the detector's implementation.

We have used only three different constellations to derive the results in this paper, namely, the 2-ring/4-ary phase, the 4-ring/4-ary phase, and the 4-PSK constellations, and we have shown that 16-QAM gives poor performance. Constellation design is thus another interesting research topic that can be addressed in future work. In particular, given a set of performance criteria, it would be interesting to find the "best" constellation that satisfies the conditions. This question is closely related to the question about metrics, since for a given power, the performance of a constellation improves by increasing the minimum distance between its points.

We did not impose any criterion for choosing equivalence-class representatives, *i.e.*, symbol blocks. It would be interesting to see if some particular elements are better than others for use as class representatives.

Although the numerical simulations revealed that the average transmitter power equals \mathcal{P}_S in the simulations, it would be interesting to generalize Theorem 1 to allow for dependent symbols. Strengthening the convergence type is another relevant problem.

No doubt many further interesting problems can be posed.

APPENDIX PROOF OF THEOREM 1

For $k \in \{0, \dots, m-1\}$ and $\ell \in \{0, \dots, m-2\}$, let the ISI-free interval \mathcal{Y}_k and the ISI-present interval \mathcal{Z}_ℓ be as given in (3) and (4), respectively. Then,

$$\frac{1}{T} \int_{-\infty}^{\infty} |\Lambda_m(t)|^2 dt = \sum_{k=0}^{m-1} G_k + \sum_{\ell=0}^{m-2} H_\ell + \zeta_m, \quad (13)$$

where $G_k \triangleq \frac{1}{T} \int_{\mathcal{Y}_k} |\Lambda_m(t)|^2 dt$, $H_\ell \triangleq \frac{1}{T} \int_{\mathcal{Z}_\ell} |\Lambda_m(t)|^2 dt$, and

$$\zeta_m = \frac{1}{T} \int_{-\infty}^0 |\Lambda_m(t)|^2 dt + \frac{1}{T} \int_{(m-\frac{1+\beta}{2})T}^{\infty} |\Lambda_m(t)|^2 dt.$$

One may see that $\mathbb{E}[G_k] = \frac{4(1-\beta)}{4-\beta} P$ and $\mathbb{E}[H_\ell] = \frac{3\beta}{4-\beta} P$.

Let \bar{G}_m and \bar{H}_{m-1} denote, respectively, the sample average of G_k and H_ℓ random variables, *i.e.*, $\bar{G}_m = \frac{1}{m} \sum_{k=0}^{m-1} G_k$ and $\bar{H}_{m-1} = \frac{1}{m-1} \sum_{\ell=0}^{m-2} H_\ell$. Then, (13) implies that

$$\frac{1}{mT} \int_{-\infty}^{\infty} |\Lambda_m(t)|^2 dt = \bar{G}_m + \frac{m-1}{m} \bar{H}_{m-1} + \frac{\zeta_m}{m}. \quad (14)$$

As λ_k 's are i.i.d. for $k \in \{0, \dots, m-1\}$, the G_k random variables are i.i.d. and have finite variance, where the latter is true as $\text{Var}(|\lambda_k|^2) < \infty$. As a result, by the weak law of large numbers,

$$\bar{G}_m \xrightarrow{p} \frac{4(1-\beta)}{4-\beta} P \quad \text{as } m \rightarrow \infty. \quad (15)$$

Unlike G_k 's, the H_ℓ random variables, $\ell \in \{0, \dots, m-2\}$, are dependent. However, the dependency is only between adjacent H_ℓ 's. In particular, H_i and H_j are dependent, thus, $\text{Cov}(H_i, H_j) > 0$, only if $|i-j| \leq 1$, where i and $j \in \{0, \dots, m-2\}$ and $\text{Cov}(\cdot, \cdot)$ denotes the covariance. Furthermore, as $\text{Var}(|\lambda_k|^2) < \infty$ for all $k \in \{0, \dots, m-1\}$, it implies that $\text{Cov}(H_i, H_j) < \infty$. Therefore,

$$\text{Var}(\bar{H}_{m-1}) = \frac{\sum_{i,j=0}^{m-2} \text{Cov}(H_i, H_j)}{(m-1)^2} = \mathcal{O}\left(\frac{1}{m}\right).$$

Therefore, $\lim_{m \rightarrow \infty} \text{Var}(\bar{H}_{m-1}) = 0$, and Chebyshev's inequality implies that

$$\bar{H}_{m-1} \xrightarrow{p} \frac{3\beta}{4-\beta} P \quad \text{as } m \rightarrow \infty. \quad (16)$$

Furthermore, $\text{Var}\left(\frac{\zeta_m}{m}\right) = \mathcal{O}\left(\frac{1}{m^2}\right)$; thus,

$$\frac{\zeta_m}{m} \xrightarrow{p} 0 \quad \text{as } m \rightarrow \infty. \quad (17)$$

As a result, (14), (15), (16), and (17) imply that

$$\frac{1}{mT} \int_{-\infty}^{\infty} |\Lambda_m(t)|^2 dt \xrightarrow{p} P \quad \text{as } m \rightarrow \infty.$$

ACKNOWLEDGMENT

The authors would like to thank Qun Zhang for helpful discussions regarding the split-step Fourier simulation method.

REFERENCES

- [1] C. Giacovazzo, *Phasing in Crystallography: A Modern Perspective*, 1st ed. London, UK: Oxford Univ. Press, 2014.
- [2] B. F. Burke and F. Graham-Smith, *An Introduction to Radio Astronomy*, 3rd ed. Cambridge, UK: Cambridge Univ. Press, 2009.
- [3] J. Aparici, "A wide dynamic range square-law diode detector (for radioastronomy)," *IEEE Trans. Instrum. Meas.*, vol. 37, no. 3, pp. 429–433, Sep. 1988.
- [4] G. E. Nilsson, T. Tenland, and P. Oberg, "A new instrument for continuous measurement of tissue blood flow by light beating spectroscopy," *IEEE Trans. Biomed. Eng.*, vol. BME-27, no. 1, pp. 12–19, Jan. 1980.
- [5] F. F. Digham, M. Alouini, and M. K. Simon, "On the energy detection of unknown signals over fading channels," *IEEE Trans. Commun.*, vol. 55, no. 1, pp. 21–24, Jan. 2007.
- [6] D. R. Hummels, C. Adams, and B. K. Harms, "Filter selection for receivers using square-law detection," *IEEE Trans. Aerosp. Electron. Syst.*, vol. AES-19, no. 6, pp. 871–883, Nov. 1983.
- [7] B. Xu and M. Brandt-Pearce, "Multisuser detection for square-law receiver under Gaussian channel noise with applications to fiber-optic communications," *IEEE Trans. Inf. Theory*, vol. 51, no. 7, pp. 2657–2664, Jul. 2005.

- [8] G. P. Agrawal, *Fiber-Optic Communication Systems*, 4th ed. NJ, USA: John Wiley & Sons, 2010.
- [9] S. Kumar and M. J. Deen, *Fiber Optic Communications: Fundamentals and Applications*, 1st ed. UK: John Wiley & Sons, 2014.
- [10] A. Mecozzi and M. Shtaif, "On the capacity of intensity modulated systems using optical amplifiers," *IEEE Photon. Technol. Lett.*, vol. 13, no. 9, pp. 1029–1031, Sep. 2001.
- [11] M. I. Yousefi and F. R. Kschischang, "The per-sample capacity of zero-dispersion optical fibers," in *12th Can. Workshop Inf. Theory*, Kelowna, BC, Canada, May 2011, pp. 98–101.
- [12] K. S. Turitsyn, S. A. Derevyanko, I. V. Yurkevich, and S. K. Turitsyn, "Information capacity of optical fiber channels with zero average dispersion," *Phys. Rev. Lett.*, vol. 91, no. 20, p. 203901, Nov. 2003.
- [13] I. Jacobs, "Limits on the power and spectral efficiency of direct detection systems with optical amplifiers," in *35th Asimolar Conf. Signals Syst. Comput.*, Pacific Grove, CA, USA, Nov. 2001, pp. 8–12.
- [14] L. Chen, B. Krongold, and J. Evans, "Performance analysis for optical OFDM transmission in short-range IM/DD systems," *J. Lightwave Technol.*, vol. 30, no. 7, pp. 974–983, Apr. 2012.
- [15] —, "Theoretical characterization of nonlinear clipping effects in IM/DD optical OFDM systems," *IEEE Trans. Commun.*, vol. 60, no. 8, pp. 2304–2312, Aug. 2012.
- [16] S. D. Dissanayake and J. Armstrong, "Comparison of ACO-OFDM, DCO-OFDM and ADO-OFDM in IM/DD systems," *J. Lightwave Technol.*, vol. 31, no. 7, pp. 1063–1072, Apr. 2013.
- [17] B. Karanov *et al.*, "End-to-end deep learning of optical fiber communications," *J. Lightwave Technol.*, vol. 36, no. 20, pp. 4843–4855, Oct. 2018.
- [18] K. Yonenaga and S. Kuwano, "Dispersion-tolerant optical transmission system using duobinary transmitter and binary receiver," *J. Lightwave Technol.*, vol. 15, no. 8, pp. 1530–1537, Aug. 1997.
- [19] A. V. T. Cartaxo, "Cross-phase modulation in intensity modulation-direct detection WDM systems with multiple optical amplifiers and dispersion compensators," *J. Lightwave Technol.*, vol. 17, no. 2, pp. 178–190, Feb. 1999.
- [20] X. Li, R. Mardling, and J. Armstrong, "Channel capacity of IM/DD optical communication systems and of ACO-OFDM," in *IEEE Int. Conf. Commun.*, Glasgow, UK, Jun. 2007, pp. 2128–2133.
- [21] A. Mecozzi and M. Shtaif, "Information capacity of direct detection optical transmission systems," *J. Lightwave Technol.*, vol. 36, no. 3, pp. 689–694, Feb. 2018.
- [22] A. Tasbihi and F. R. Kschischang, "On the capacity of waveform channels under square-law detection of time-limited signals," *IEEE Trans. Info. Theory*, vol. 66, no. 11, pp. 6682–6687, Nov. 2020.
- [23] A. Mecozzi, C. Antonelli, and M. Shtaif, "Kramers–Kronig coherent receiver," *Optica*, vol. 3, no. 11, pp. 1220–1227, 2016.
- [24] Z. Li *et al.*, "SSBI mitigation and the Kramers–Kronig scheme in single-sideband direct-detection transmission with receiver-based electronic dispersion compensation," *J. Lightwave Technol.*, vol. 35, no. 10, pp. 1887–1893, May 2017.
- [25] X. Chen *et al.*, "218-Gb/s single-wavelength, single-polarization, single-photodiode transmission over 125-km of standard singlemode fiber using Kramers–Kronig detection," in *Proc. Opt. Fiber Commun. Conf. Expo. (OFC)*, Los Angeles, CA, USA, Mar. 2017, pp. Th5B.6:1–3.
- [26] —, "Kramers–Kronig receivers for 100-km datacenter interconnects," *J. Lightwave Technol.*, vol. 36, no. 1, pp. 79–89, Jan. 2018.
- [27] Z. Li *et al.*, "Joint optimisation of resampling rate and carrier-to-signal power ratio in direct-detection Kramers–Kronig receivers," in *Eur. Conf. Opt. Commun. (ECOC)*, Gothenburg, Sweden, Sep. 2017, pp. 1–3.
- [28] A. Lender, "The duobinary technique for high-speed data transmission," *IEEE Trans. Commun. Electron.*, vol. 82, no. 2, pp. 214–218, May 1963.
- [29] E. Kretzmer, "Generalization of a technique for binary data communication," *IEEE Trans. Commun. Technol.*, vol. 14, no. 1, pp. 67–68, Feb. 1966.
- [30] F. K. Becker, E. R. Kretzmer, and J. R. Sheehan, "A new signal format for efficient data transmission," *Bell Syst. Tech. J.*, vol. 45, no. 5, pp. 755–758, May-Jun. 1966.
- [31] J. Smith, "Error control in duobinary data systems by means of null zone detection," *IEEE Trans. Commun. Technol.*, vol. 16, no. 6, pp. 825–830, Dec. 1968.
- [32] J. Gunn and J. Lombardi, "Error detection for partial-response systems," *IEEE Trans. Commun. Technol.*, vol. 17, no. 6, pp. 734–737, Dec. 1969.
- [33] H. Kobayashi and D. Tang, "On decoding of correlative level coding systems with ambiguity zone detection," *IEEE Trans. Commun. Technol.*, vol. 19, no. 4, pp. 467–477, Aug. 1971.
- [34] P. Kabal and S. Pasupathy, "Partial-response signalling," *IEEE Trans. Commun.*, vol. 23, no. 9, pp. 921–934, Sep. 1975.
- [35] H. Kobayashi and D. Tang, "Application of partial-response channel coding to magnetic recording systems," *IBM J. Res. Dev.*, vol. 14, no. 4, pp. 368–375, Jul. 1970.
- [36] R. Wood and D. Petersen, "Viterbi detection of class IV partial response on a magnetic recording channel," *IEEE Trans. Commun.*, vol. COM-34, no. 5, pp. 454–461, May 1986.
- [37] H. Thapar and A. Patel, "A class of partial response systems for increasing storage density in magnetic recording," *IEEE Trans. Magn.*, vol. 23, no. 5, pp. 3666–3668, Sep. 1987.
- [38] J. E. Mazo, "Faster-than-Nyquist signaling," *Bell Syst. Techn. J.*, vol. 54, no. 8, pp. 1451–1462, Oct. 1975.
- [39] G. Colavolpe, T. Foggi, A. Modenini, and A. Piemontese, "Faster-than-Nyquist and beyond: How to improve spectral efficiency by accepting interference," *Optics Expr.*, vol. 19, no. 27, pp. 26 600–26 609, Dec. 2011.
- [40] J. B. Anderson, F. Rusek, and V. Öwall, "Faster-than-Nyquist signaling," *Proc. IEEE*, vol. 101, no. 8, pp. 1817–1830, Aug. 2013.
- [41] M. Jana, A. Medra, L. Lampe, and J. Mitra, "Pre-equalized faster-than-Nyquist transmission," *IEEE Trans. Commun.*, vol. 65, no. 10, pp. 4406–4418, Oct. 2017.
- [42] H. Bülow, F. Buchali, and A. Klekamp, "Electronic dispersion compensation," *J. Lightwave Technol.*, vol. 26, no. 1, pp. 158–167, Feb. 2008.
- [43] M. M. E. Said, J. Sitch, and M. I. Elmasry, "An electrically pre-equalized 10-Gb/s duobinary transmission system," *J. Lightwave Technol.*, vol. 23, no. 1, pp. 388–400, Jan. 2005.
- [44] R. I. Killey, P. M. Watts, V. Mikhailov, M. Glick, and P. Bayvel, "Electronic dispersion compensation by signal predistortion using digital processing and a dual-drive Mach-Zehnder modulator," *IEEE Photon. Technol. Lett.*, vol. 17, no. 3, pp. 714–716, Mar. 2005.
- [45] J. Zhou *et al.*, "Transmission of 100-Gb/s DSB-DMT over 80-km SMF using 10-G class TTA and direct-detection," in *Eur. Conf. Opt. Commun. (ECOC)*, Dusseldorf, Germany, Sep. 2016, pp. 1–3.
- [46] D. McGhan, C. Laperle, A. Savehenko, C. Li, G. Mak, and M. O'Sullivan, "5120 km RZ-DPSK transmission over G652 fiber at 10 Gb/s with no optical dispersion compensation," in *Proc. Opt. Fiber Commun. Conf. Expo. (OFC)*, Anaheim, CA, USA, Mar. 2005, pp. PDP27:1–3.
- [47] M. Tomlinson, "New automatic equalizer employing modulo arithmetic," *Electron. Lett.*, vol. 7, pp. 138–138, Mar. 1971.
- [48] M. Miyakawa and H. Harashima, "A method of code conversion for a digital communication channel with intersymbol interference," *Trans. Inst. Electron. Commun. Eng. Japan*, vol. 52-A, pp. 272–273, Jun. 1969.
- [49] W. Yu, D. P. Varodayan, and J. M. Cioffi, "Trellis and convolutional precoding for transmitter-based interference presubtraction," *IEEE Trans. Commun.*, vol. 53, no. 7, pp. 1220–1230, Jul. 2005.
- [50] E. A. Robinson, "A historical perspective of spectrum estimation," *Proc. IEEE*, vol. 70, no. 9, pp. 885–907, Sep. 1982.
- [51] J. W. Tukey, "An introduction to the calculations of numerical spectrum analysis," in *Spectral Analysis of Time Series*, B. Harris, Ed. New York, USA: John Wiley & Sons, 1967, pp. 25–46.
- [52] N. Geckinli and D. Yavuz, "Some novel windows and a concise tutorial comparison of window families," *IEEE Trans. Acoust., Speech, Signal Process.*, vol. 26, no. 6, pp. 501–507, Dec. 1978.
- [53] F. J. Harris, "On the use of windows for harmonic analysis with the discrete Fourier transform," *Proc. IEEE*, vol. 66, no. 1, pp. 51–83, Jan. 1978.
- [54] F. R. Kschischang, B. J. Frey, and H. A. Loeliger, "Factor graphs and the sum-product algorithm," *IEEE Trans. Info. Theory*, vol. 47, no. 2, pp. 498–519, Feb. 2001.
- [55] G. Ungerboeck, "Channel coding with multilevel/phase signals," *IEEE Trans. Info. Theory*, vol. 28, no. 1, pp. 55–67, Jan. 1982.
- [56] G. P. Agrawal, *Nonlinear Fiber Optics*, 6th ed. Academic Press, 2019.
- [57] E. Ip and J. M. Kahn, "Compensation of dispersion and nonlinear impairments using digital backpropagation," *J. Lightwave Technol.*, vol. 26, no. 20, pp. 3416–3425, Oct. 2008.
- [58] A. E. Stevens, "An integrate-and-dump receiver for fiber optic networks," Ph.D. dissertation, Columbia University, New York, NY, USA, 1995.
- [59] T. Bo and H. Kim, "Kramers–Kronig receiver operable without digital upsampling," *Opt. Express*, vol. 26, no. 11, pp. 13 810–13 818, May 2018.
- [60] —, "Toward practical Kramers–Kronig receiver: Resampling, performance, and implementation," *J. Lightwave Technol.*, vol. 37, no. 2, pp. 461–469, Jan. 2019.
- [61] D. R. Brillinger, "John W. Tukey: his life and professional contributions," *Ann. Statist.*, vol. 30, no. 6, pp. 1535–1575, Dec. 2002.